Supplementary Information

Stabilizing lithium into cross-stacked nanotube sheets with ultra-high specific capacity for lithium oxygen battery

Lei Ye[†], *Meng Liao*[†], *Hao Sun, Yifan Yang, Chengqiang Tang, Yang Zhao, Lie Wang, Bingjie Wang, Fan Xu, Xuemei Sun, Ye Zhang*, Hongjie Dai, Peter G. Bruce and Huisheng Peng**

*Corresponding author. E-mail: penghs@fudan.edu.cn (Huisheng Peng)

This PDF file includes:

Supplementary Notes

1. Preparation of 3D cross-stacked carbon nanotube network (3D-CSC)

The 3D-CSC was drawn from a spinnable carbon nanotube (CNT) array and cross-stacked layer by layer orthogonally. The spinnable CNT array was synthesized through a chemical vapor deposition process. Fe (1.2 nm) and Al_2O_3 (3 nm) were deposited on a silicon wafer as catalysts. Then ethylene with a flowing rate of 90 sccm was used as the carbon source, and a mixture of Ar (400 sccm) and H_2 (30 sccm) was used as the carrier gas. The spinnable CNT array with thickness of ~200 μm was obtained at a growth temperature of 750 °C. Aligned CNT sheets with a thickness of ~20 nm for each layer were drawn from the CNT array and then paved onto polytetrafluoroethylene substrate with a stacking angle of 90° between two neighboring layers. In a typical fabrication, the adopted 3D-CSC in this work was comprised of 50 layers of aligned CNT sheets (total thickness of ~1 μm). The free-standing 3D-CSC was then cut into electrodes with diameter of 1 cm.

2. Synthesis of the Li/3D-CSC anode

The 3D-CSC was assembled into CR2032 coin cells with Li foils as the counter/reference electrode in Argon-filled glove box without additional current collectors. The 1 M lithium bis(trifluoromethanesulfonyl)imide in 1,3-dioxolane (DOL)/1,2-dimethoxyethane (DME) (1:1 w/w) with 1 wt% lithium nitrate electrolyte was used as received. The assembled cell contained the above electrolyte of ~30 μL. Before Li electroplating and further electrochemical measurements, an activation process was conducted. In detail, symmetric cells were first cycled between 0 and 0.5 V (*versus* Li/Li^+) at a current density of 0.1 mA/cm^2 for 4 cycles to remove impurities and form stable solid electrolyte interface (SEI). A constant current density of 0.5 mA/cm^2 was then applied to electrodeposit metallic Li into the 3D-CSC to produce the Li/3D-CSC. The 'loading' and 'further loading' status of Li in Figure 2a corresponded to Li loading capacity of 1 and 2 mAh/cm^2, respectively.

3. Electrochemical measurements of Li/3D-CSC anodes

Symmetric cells from Li/3D-CSC and Li foil electrodes were employed for evaluating their Coulomb efficiency (CE), long cycle ability, voltage hysteresis and rate performance. CR2032 cells were assembled in an Argon-filled glove box ($H_2O < 0.1$ ppm, $O_2 < 0.1$ ppm) with 1 M lithium bis(trifluoromethanesulfonyl)imide in 1,3-dioxolane (DOL)/1,2-dimethoxyethane (DME) (1:1 w/w) with 1 wt% lithium nitrate as electrolyte and Celgard 2400 as separator. Each symmetric cell contained

~30 μL electrolyte. For the control samples, Cu foil and bare Li foil were employed to replace the 3D-CSC, making symmetric cells with the other conditions to be the same. Note that the above-mentioned activation process was conducted before all the electrochemical measurements of Li/3D-CSC anodes.

To test the CE evolution of Li/3D-CSC, different capacities of metal Li were plated onto the electrodes at a current density of 0.5 mA/cm^2 by varying the depositing time. After that, the cells were galvanostatically charged to 0.5 V (Li stripping process), followed by a time-controlled discharge process to plate metal Li at 0.5, 1.0 and 2.0 mA/cm^2, respectively. To test the long-term stability and voltage hysteresis, the same activation and deposition processes were employed in symmetric cells as described above, followed by galvanostatic plating and stripping of metal Li at a given Li deposition capacity. The electrochemical impedance spectroscopy (EIS) test was carried out on a CHI 660D electrochemical workstation with a frequency range from 10^{-2} Hz to 10^5 Hz and an amplitude of 5 mV. The open-circuit potential was set as the initial voltage. The calculation of specific capacity for Li/3D-CSC was made according to the previous study.[S7,S8] Taking an Li/3D-CSC (electrode geometric area of 1 cm^2) with areal Li loading capacity of 5 mAh/cm^2 for example, here the total accommodated Li mass (259 μg/mAh) was 259 μg/mAh × 5 mAh = 1295 μg. In this work the mass of 3D-CSC (scaffold) was 72.5 μg. The accommodation ratio of the Li/3D-CSC anode was $m_{Li}/(m_{Li}+m_{scaffold})$=1295 μg /(72.5 μg +1295 μg)= 0.947. Thus the specific capacity of the Li/3D-CSC was 3861 mAh/g × 0.947 = 3656 mAh/g.

4. Simulation of the electric field regulation in Ansoft Maxwell

The simulation mainly focused on the electric field regulation on the anode surface in the initial Li deposition stage. Simulation cell geometry in Ansoft Maxwell for Li/Cu foil anode and Li/3D-CSC anode were presented in Figures 4a and b. The two-dimensional electrodeposition models based on the electrode structures (i.e., planar Cu foil and 3D-CSC with periodic voids) were used to compare the proportional schematics of electric field distribution during recurring Li plating/stripping. The length of the entire model was 15 μm and the height of electrolyte was set to 50 μm. The ionic conductivity of 1 M LiTFSI in 1:1 DOL:DME was set to 1.1 S/m. The model of Li/3D-CSC was depicted according to its sectional view and the 3D-CSC skeleton was set with diameter of 200 nm and height of 200 nm. The interval between the neighboring two CNT bundles in the same layer was about 200 nm. The thickness of entire metallic Li was 15 μm. The existing nuclei were assumed to have diameters of ~200 nm and heights of ~200 nm. The maximal spilt unit length for the mesh portioning of the model was 50 nm. The electrical conductivities of the 3D-CSC, Cu foil and Li metal were 1.0×10^6, 5.7×10^7 and

1.17×10^7 S/m, respectively. The overpotential of 500 mV was employed as voltage excitation between the anode and electrolyte sides, and the remaining boundary was chosen as Bolloon type during simulation.

5. Preparation of the other carbon nanotube anodes

The preparation of the stacked CNT anode with angle of 45° between two neighboring CNT sheets was the same to the 3D-CSC, and the CNT sheets can be also paved to be parallel (i.e., 0° between the two neighboring CNT sheets). To prepare the randomly dispersed CNT anode, commercial CNT dispersion was cast onto a Cu foil current collector by a simple spin-coating process (rotating speed: 4000 r/s, time: 30 s). The composite film was then punched into circular disks with diameters of ~1.25 cm. The obtained randomly dispersed CNT network presented a mass load of ~2.4 mg/cm^2.

6. The von Mises stress distribution simulation

The simulation mainly focused on the inner stress durability and distribution of different CNT scaffolds at the given Li deposition height. The model was built with finite element software ABAQUS. In the model, several silver balls representing Li protrusion (diameter of 200 nm) was applied at different CNT-based scaffolds. The silver balls were raised up imitating the Li dendrite growth from inner space. To simplify the models, aligned CNT bundles in 3D-CSC, 0-CNT and 45°-CNT were set with a length of 2.2 μm and a width of 100 nm. The Young modulus and Possion ratio for aligned CNT bundle were 10 GPa and 0.15-0.35, respectively. For the R-CNT scaffold, CNT bundles were set with a length of 600 nm and a width of 100 nm, respectively. The modulus and Possion ratio for them were 520 MPa and 0.15–0.35, respectively.

7. Fabrication and cyclic test of lithium-oxygen batteries based on Li/3D-CSC and bare Li foil anodes

To prepare the cathodes in Li-O_2 batteries, 10 layers of aligned CNT sheets drawn from a spinnable CNT array were used as the cathode of the Li-O_2 battery without any other modification. The fabricated cathode exhibited a geometric area of ~1 cm^2 and a mass load of 14.1 μg. The electrolyte was obtained by dissolving 0.318 g lithium triflate and 0.0134 g lithium iodide in 2.018 g tetraethylene glycol dimethyl ether (TEGDME). Molecular sieves (4 A) were added to remove water for 24 h before use. The 3D-CSC/Li or bare Li foil anode, electrolyte, separator (glass fiber, Whatman GF/A) and cathode were assembled in sequence in Swagelok-type Li-O_2 battery for electrochemical test and comparison. To standardize the test, 60 μL electrolyte was used for each Li-O_2 battery. The Li-O_2 batteries were tested in dry oxygen atmosphere (relative humidity of less than 5%) with a fixed capacity of 1000 mAh/g at 2000 mA/g. The specific capacity (C) was calculated by $C = (I \times t)/m$, where I, t, and m represent the discharge current, discharge time and mass of the air electrode, respectively.

8. Materials

The 1 M lithium bis(trifluoromethanesulfonyl)imide in 1,3-dioxolane (DOL)/1,2-dimethoxyethane (DME) (1:1, w/w) with 1 wt % lithium nitrate electrolyte was ordered from Shanghai Xiaoyuan Energy Co. Ltd. Cu and Al foils were obtained from Shenzhen Kejing Star Technology Corporation. Li foil was ordered from China Energy Lithium Co. Ltd. The Celgard 2400 separator was obtained from Celgard Co. Ltd. $LiFePO_4$, Super P, polyvinylidene fluoride (PVDF), TEGDME were obtained from Sinopharm and used as received. N-methyl-2-pyrrolidone (NMP) was ordered from Aladdin. Lithium triflate and lithium iodide were obtained from Sigma-Aldrich. CNT dispersion was obtained from Chengdu Organic Chemicals Co., Ltd., Chinese Academy of Science. The Whatman G/F A separator was obtained from Whatman Co. Ltd.

9. Characterization

The 3D-CSC/Li, Cu/Li and Li foil electrodes were extracted out from the coin cells for further characterization. Before analysis, the electrodes were rinsed in DOL solvent twice to remove residual electrolyte and then dried in glove box. The structure was characterized by scanning electron microscopy (SEM, Hitachi FE-SEM S-4800 operated at 1 kV, Zeiss FE-SEM Ultra 55 operated at 3 kV and FIB-SEM Zeiss Auriga operated at 5 kV), transmission electron microscopy (TEM, JEOL JEM-2100F operated at 200 kV), atomic force microscopy (Multimode 8), Raman spectroscopy (Dilor LabRam-1B, He-Ne laser of 4 mW, excitation wavelength of 632.8 nm), X-ray diffraction (Bruker AXSD8), X-ray photoelectron spectroscopy (PHI5000C & PHI5300, Mg, 250 W, 14 kV), automatic specific surface area and porosity analyzer (Quadrasorb evo). The electrochemical performances were obtained from an Arbin electrochemical station (MSTATS-5V/10 mA/16Ch) and CHI 660D electrochemical workstation. The optical photographs were taken by a camera (SONY A6000, Japan).

Supplementary Figures

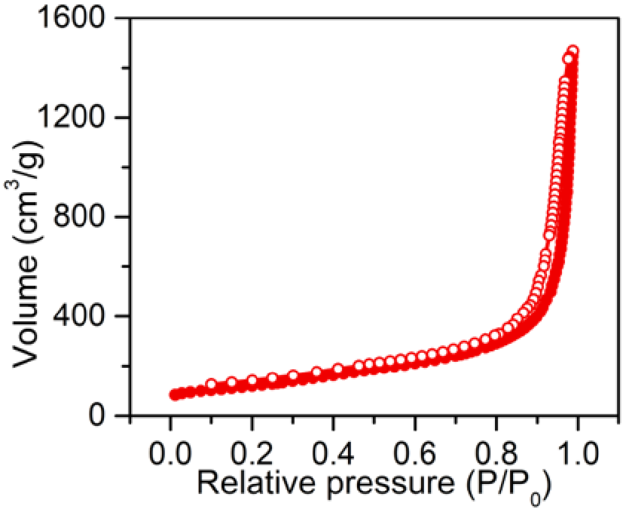

Figure S1. Nitrogen adsorption-desorption isotherm of the 3D-CSC with a high specific surface area of 424.4 m^2/g.

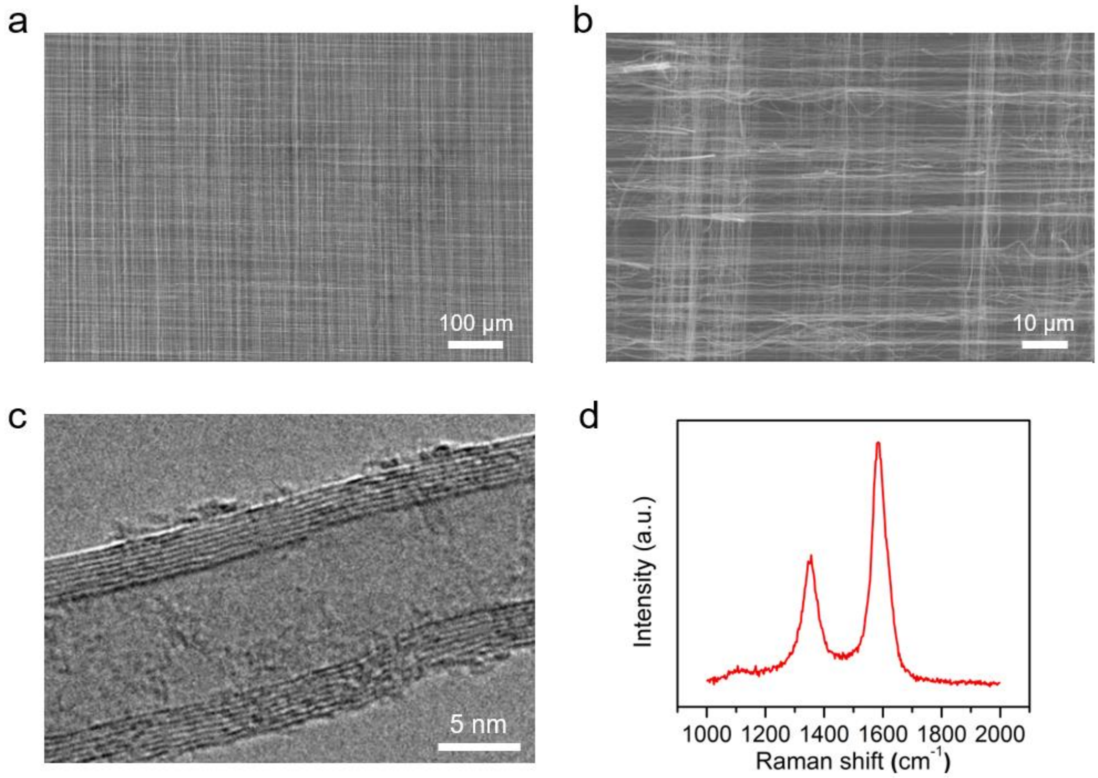

Figure S2. a and **b**, The pristine morphology of the 3D-CSC before electrolyte soaking and cycling, respectively. **c**, Transmission electron microscopy (TEM) image of CNTs employed in this work. **d**, Raman spectrum of the pristine 3D-CSC. Two characteristic bands of carbon, the D band (defect mode) at 1355 cm^{-1} and the G band (graphite mode) at 1585 cm^{-1}, were presented.

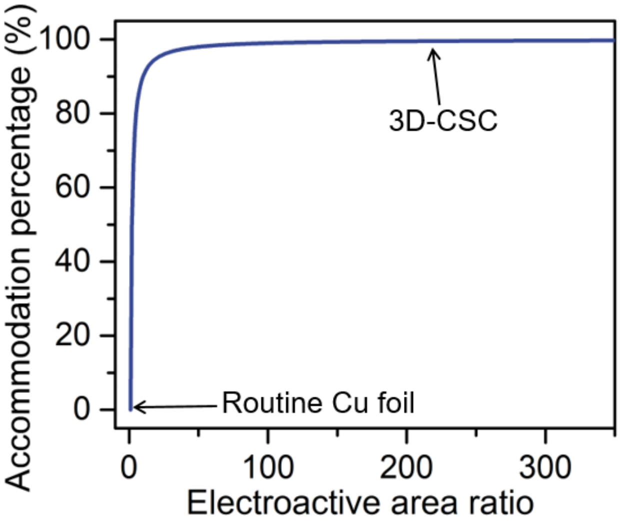

Figure S3. The 3D-CSC with porous structure demonstrating an electroactive area ratio over 98% compared to that of 0% from routine planar Cu foil.

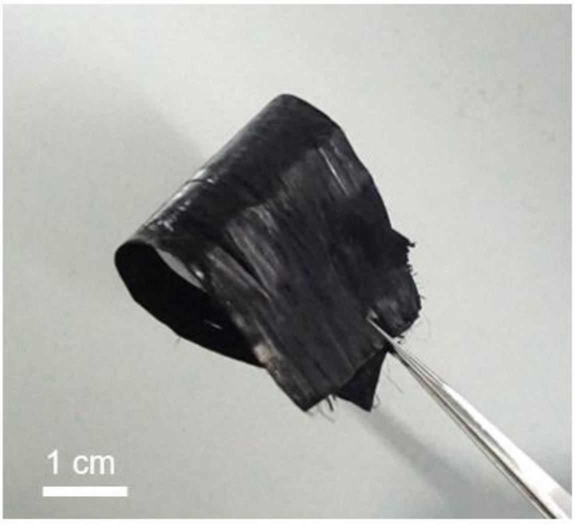

Figure S4. Free-standing 3D-CSC with high flexibility.

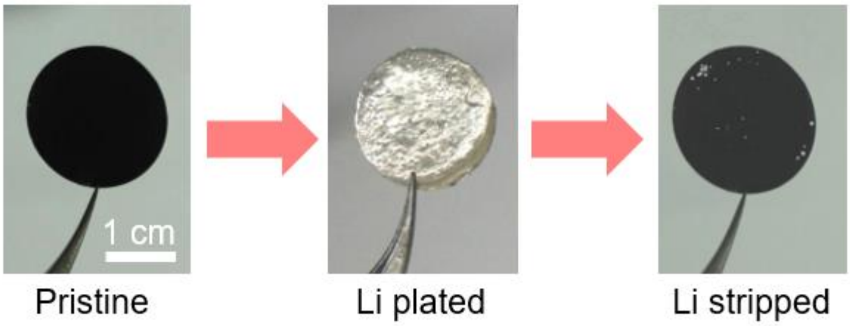

Figure S5. Photograph of pristine 3D-CSC, Li plated 3D-CSC (Li/3D-CSC) and stripped 3D-CSC.

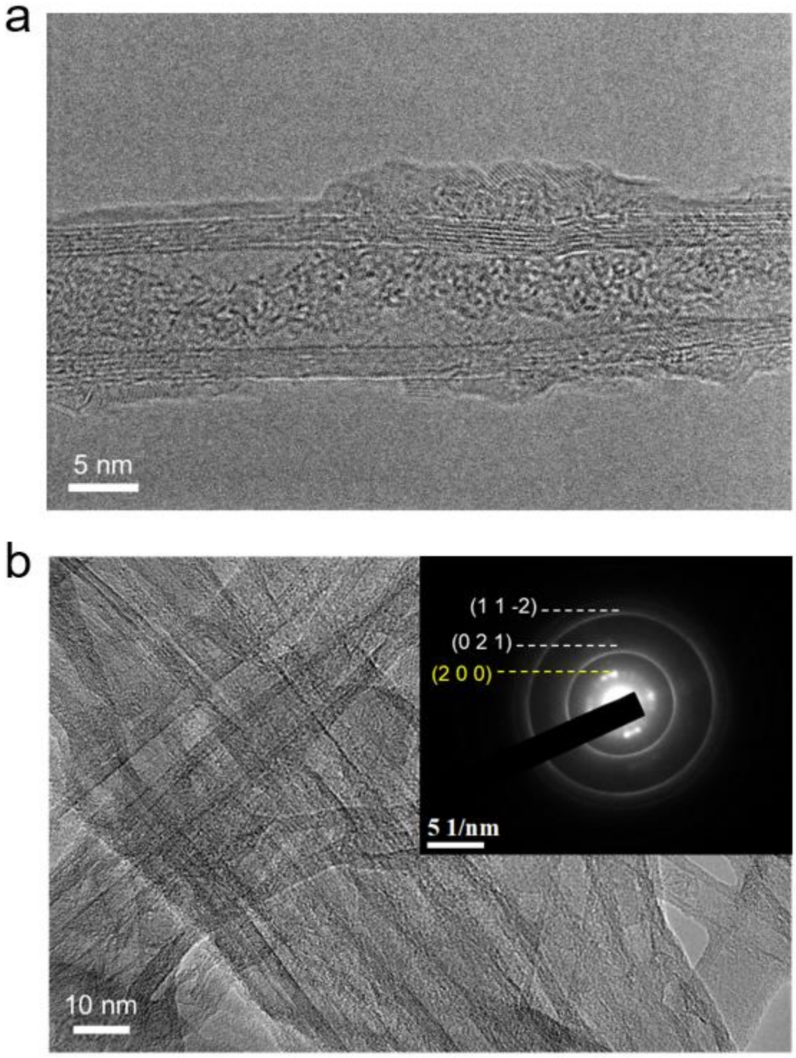

Figure S6. **a**, *ex-situ* TEM image of a CNT from Li/3D-CSC anode at initially-electroplated stage (~0.5 mAh/cm^2). The deposited Li nanoparticles firstly emerged at the CNT surface. **b**, *ex-situ* TEM image from the same Li/3D-CSC in **a** with selected area electron diffraction pattern. The diffraction rings were corresponding to the (1 1 2), (0 2 1) planes of Li_2CO_3 and (2 0 0) plane of LiOH, verifying the deposited Li nanoparticles on the CNT surface in **a**.

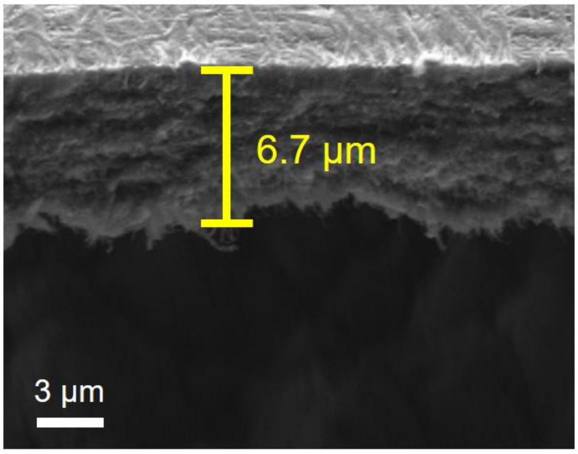

Figure S7. Cross-sectional SEM images of the 3D-CSC (initial thickness of 1.1 μm) with Li capacity of 1 mAh/cm^2.

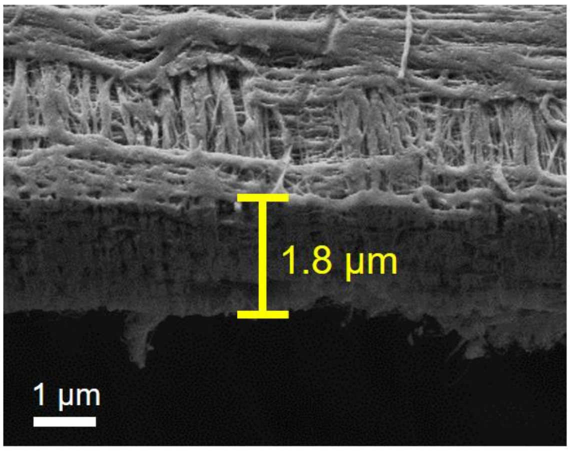

Figure S8. Cross-sectional SEM image of the stripped 3D-CSC after cycles. The thickness of 3D-CSC slightly increased compared with its pristine status (~1.1 μm).

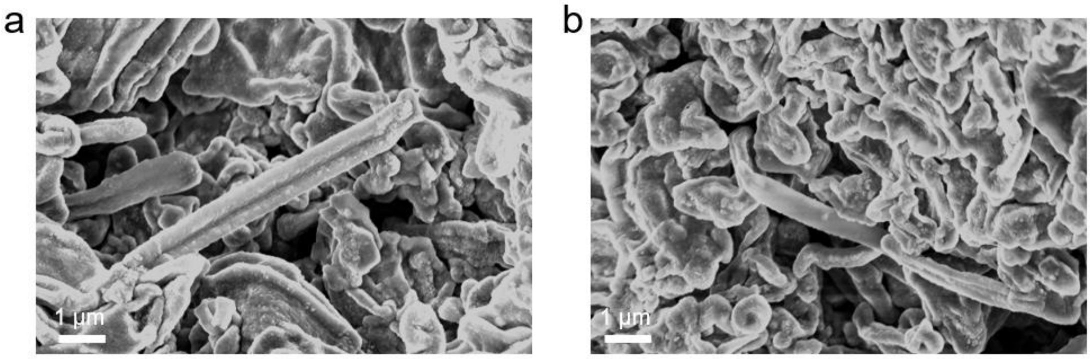

Figure S9. Scanning electron microscopy (SEM) images of the Cu foil electrode at 1 mAh/cm^2. The dendritic Li could be clearly observed.

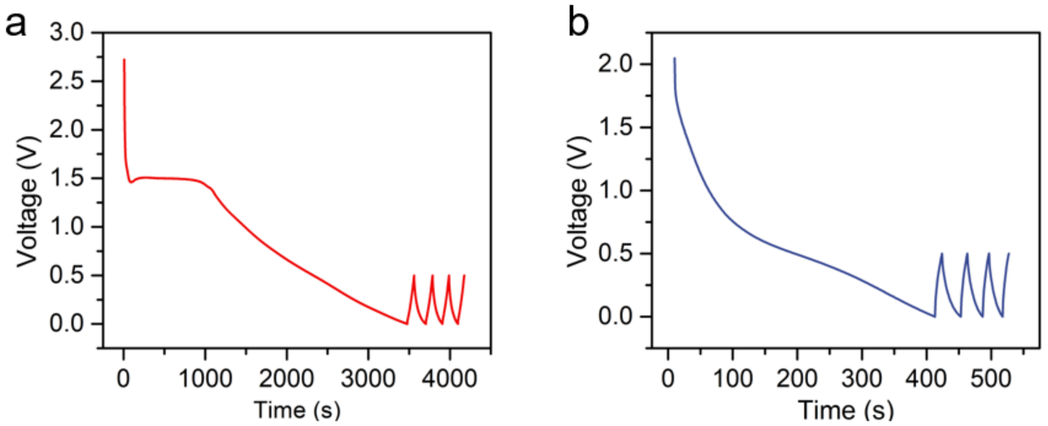

Figure S10. a and **b**, The activation process of the 3D-CSC and Cu foil, respectively. The 3D-CSC delivered a longer activation process compared with that of Cu foil, suggesting a larger electrochemical active area and more initially-formed SEI on 3D-CSC. This activation process was important for a high initial CE.

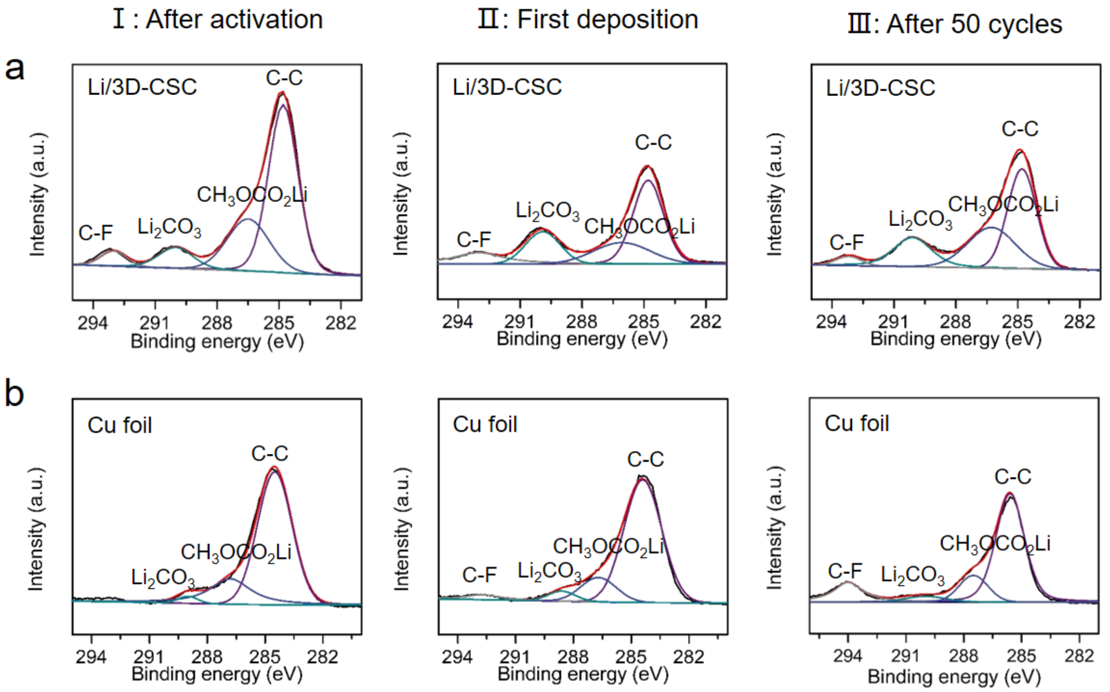

Figure S11. **a** and **b**, X-ray photoelectron spectroscopy analysis (C 1s) of the SEI on 3D-CSC and Cu foil during different cycling stages (I, after activation process; II, after first cycle of Li deposition and III, after 50 cycles of Li plating/stripping), respectively. The corresponding elemental composition variations of two anodes were provided in Table S1. For the Cu foil, larger proportions of C-F were evidenced from stage II to III, suggesting the electrolyte decomposition and unstable SEI during cycling. In contrast, for the 3D-CSC, initial SEI formed after activation process (stage I) and this as-formed SEI kept almost unchanged during the later cycling (from stage II to III), indicating the stabilized SEI on Li/3D-CSC anode.

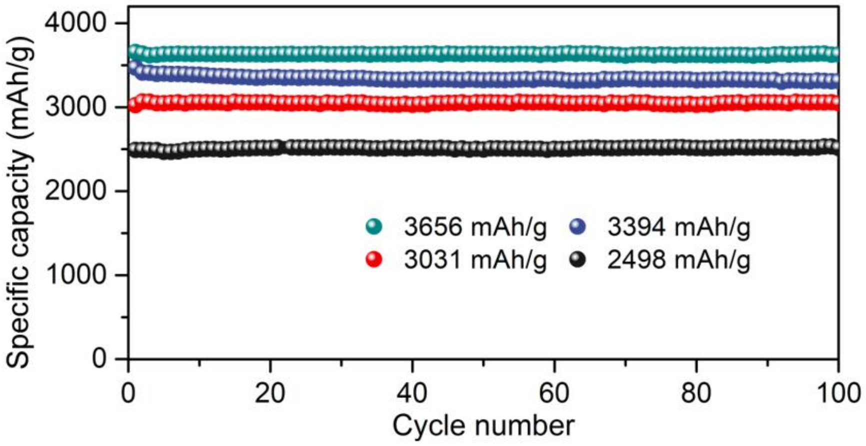

Figure S12. Cycling stability of different specific capacity anodes expressed as gravimetric capacity *versus* cycle number.

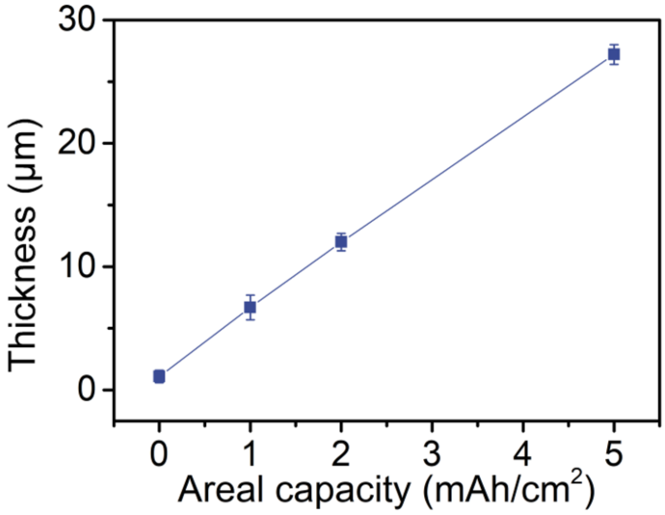

Figure S13. The dependence of the electrode thickness on the areal capacity of Li loading. Here the initial thickness of 3D-CSC was 1 μm.

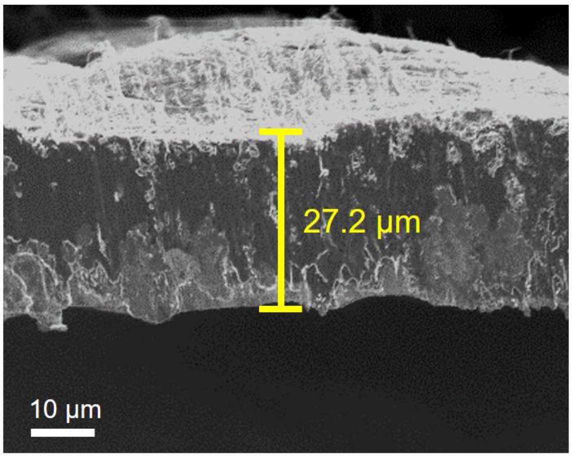

Figure S14. Cross-sectional SEM images of the 3D-CSC (initial thickness of 1.1 μm) with Li capacity of 5 mAh/cm^2.

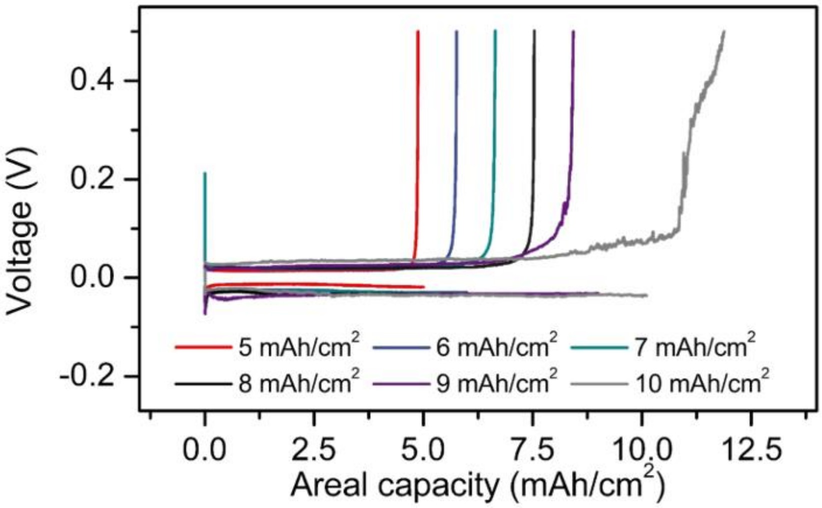

Figure S15. Li storage capacities of the 3D-CSC (initial thickness of 1.1 μm) from 5 to 10 mAh/cm^2. Note here that when the areal capacity was over 5 mAh/cm^2 (i.e., 6-10 mAh/cm^2), the corresponding CE decreased to below 99%, indicating the lowered reversibility of the obtained anodes. Since the CE was expected to be higher than 99% to enable a Li metal based battery with considerable lifespan,[S25] the maximum Li deposition capacity of this 3D-CSC was 5 mAh/cm^2 or 3656 mAh/g. The same standard was also adopted to evaluate the maximum capacity of other 3D-CSC with varying thickness.

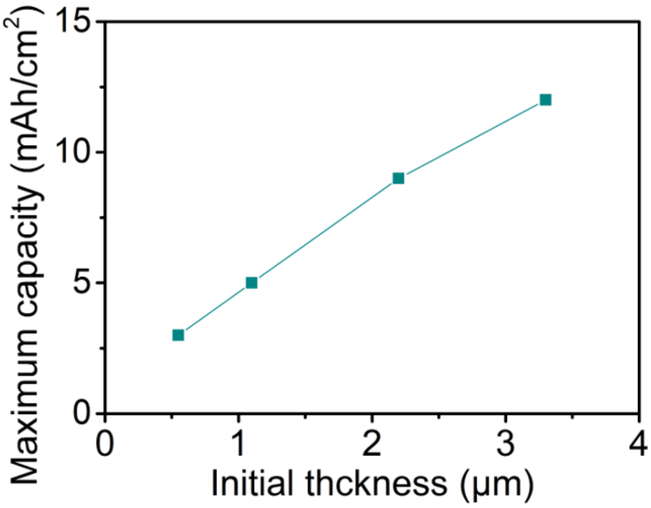

Figure S16. The dependence of the maximum Li capacity on the initial thickness of 3D-CSC.

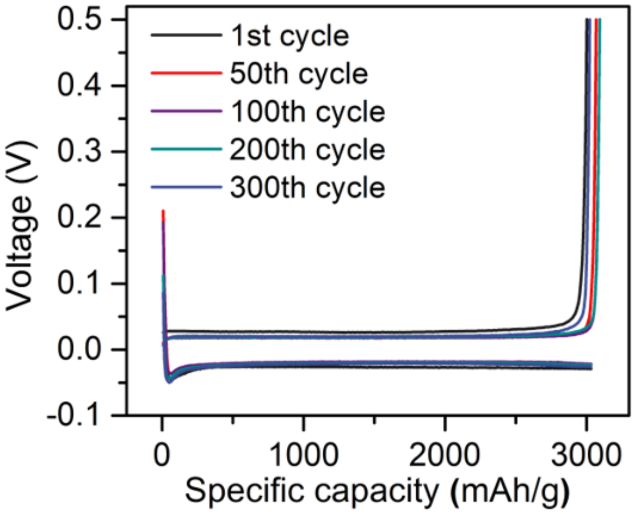

Figure S17. Voltage profiles of the Li plating/stripping process with Li metal as the reference/counter electrode at 3 A/g (1 mA/cm^2) for 3031 mAh/g (1 mAh/cm^2).

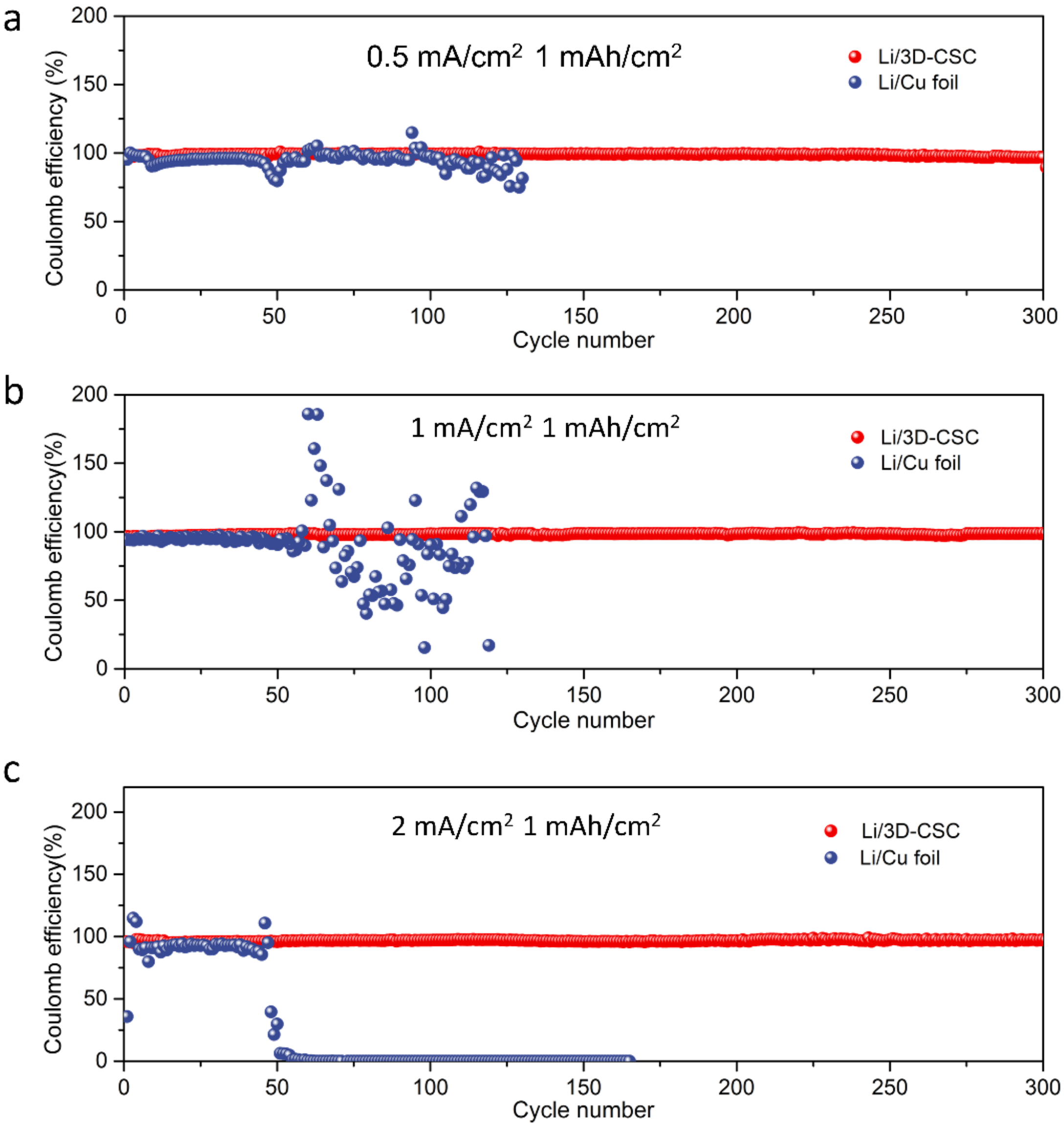

Figure S18. a-c, Cycling performance of the 3D-CSC and Cu foil at 0.5 mA/cm^2, 1 mA/cm^2 and 2 mA/cm^2 with a fixed specific area capacity of 1 mAh/cm^2.

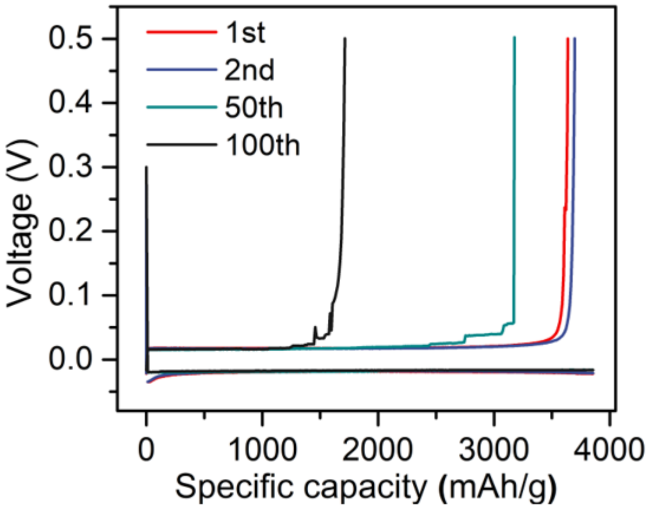

Figure S19. The plating/stripping curves at increasing cycles of the Li/Cu foil at 1 mA/cm^2 and 1 mAh/cm^2.

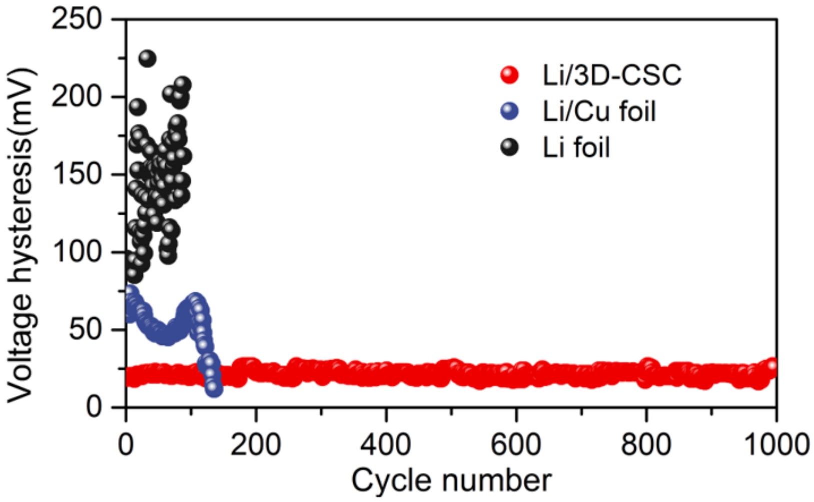

Figure S20. The voltage hysteresis of the Li/3D-CSC, Li/Cu foil and Li foil in symmetric batteries (1 mA/cm^2, 1 mAh/cm^2).

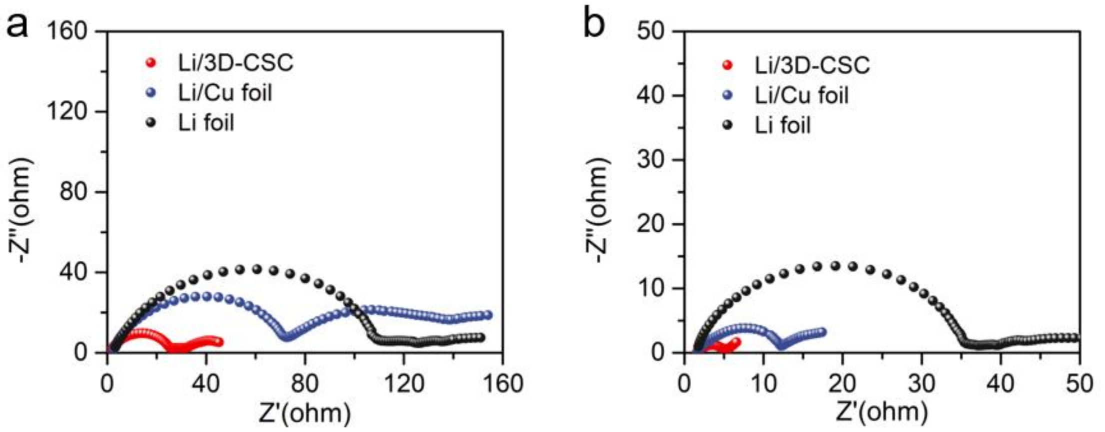

Figure S21. a and **b**, Nyquist plots of the Li/3D-CSC, Li/Cu foil and Li foil before and after 10 cycles of Li plating/stripping (1 mA/cm^2 and 1 mAh/cm^2).

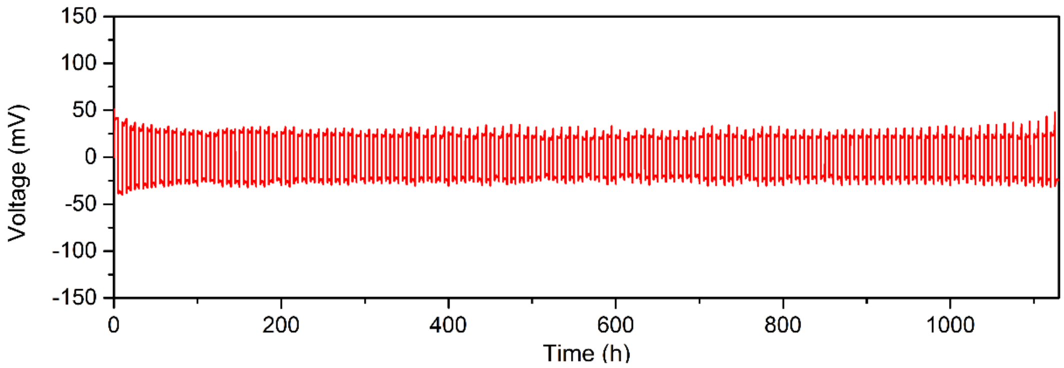

Figure S22. The voltage profiles of Li/3D-CSC in symmetric batteries at 3 A/g (1 mA/cm^2) and 3656 mAh/g (5 mAh/cm^2). The relatively low overpotential could be maintained during cycling at the ceiling specific capacity of the Li/3D-CSC anode.

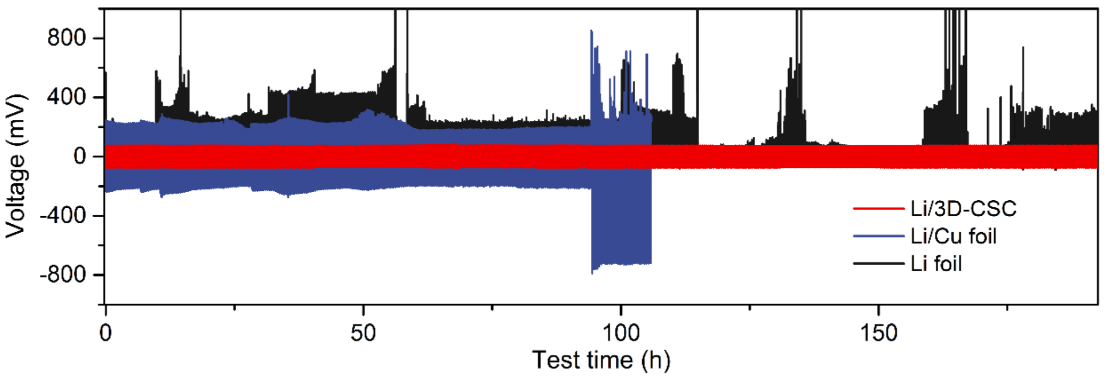

Figure S23. The voltage profiles of the Li/3D-CSC, Li/Cu foil and Li foil in symmetric batteries at 5 mA/cm^2 and 1 mAh/cm^2.

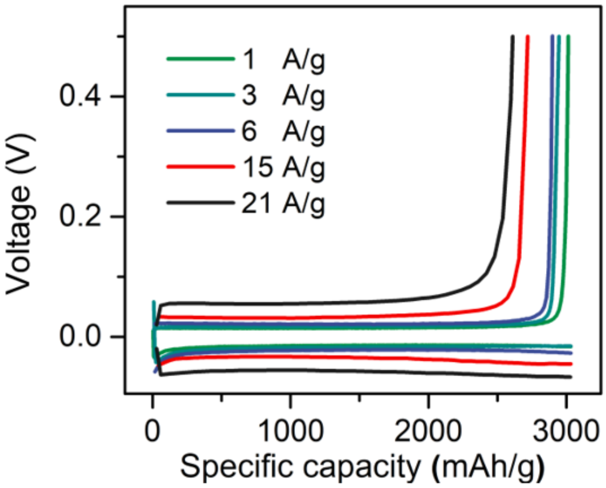

Figure S24. Charge-discharge profiles measured at different current densities.

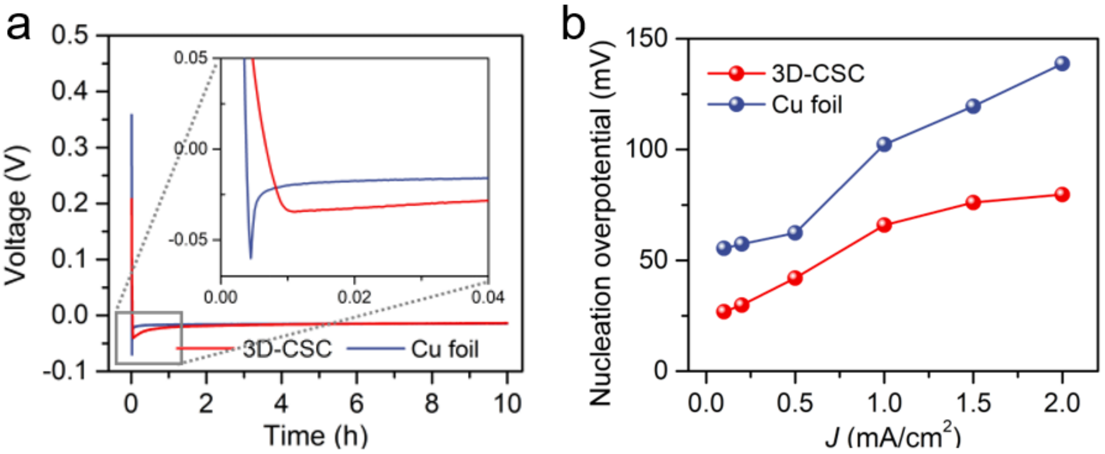

Figure S25. **a**, The voltage-time curves during Li nucleation at 0.1 mA/cm^2 on 3D-CSC and Cu foil electrodes. **b**, The Li nucleation overpotentials ($\boldsymbol{\mu_n}$) on 3D-CSC and Cu foil at different current densities.

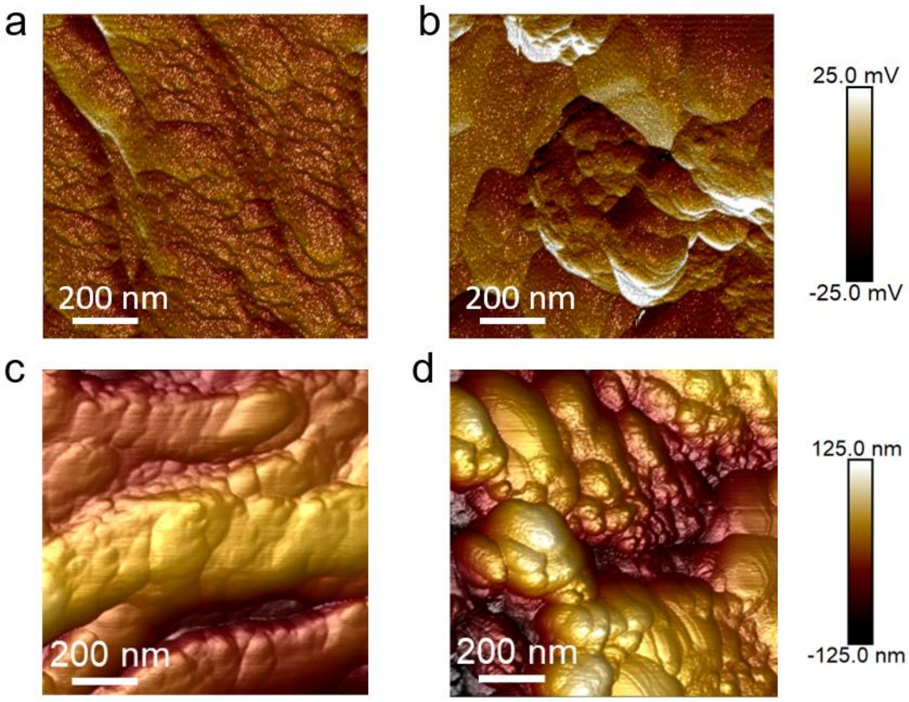

Figure S26. **a** and **b**, Atomic force microscopy (AFM) surface potential distributions of Li/3D-CSC and bare Li foil, respectively. **c** and **d**, AFM height distributions of Li/3D-CSC and bare Li foil, respectively.

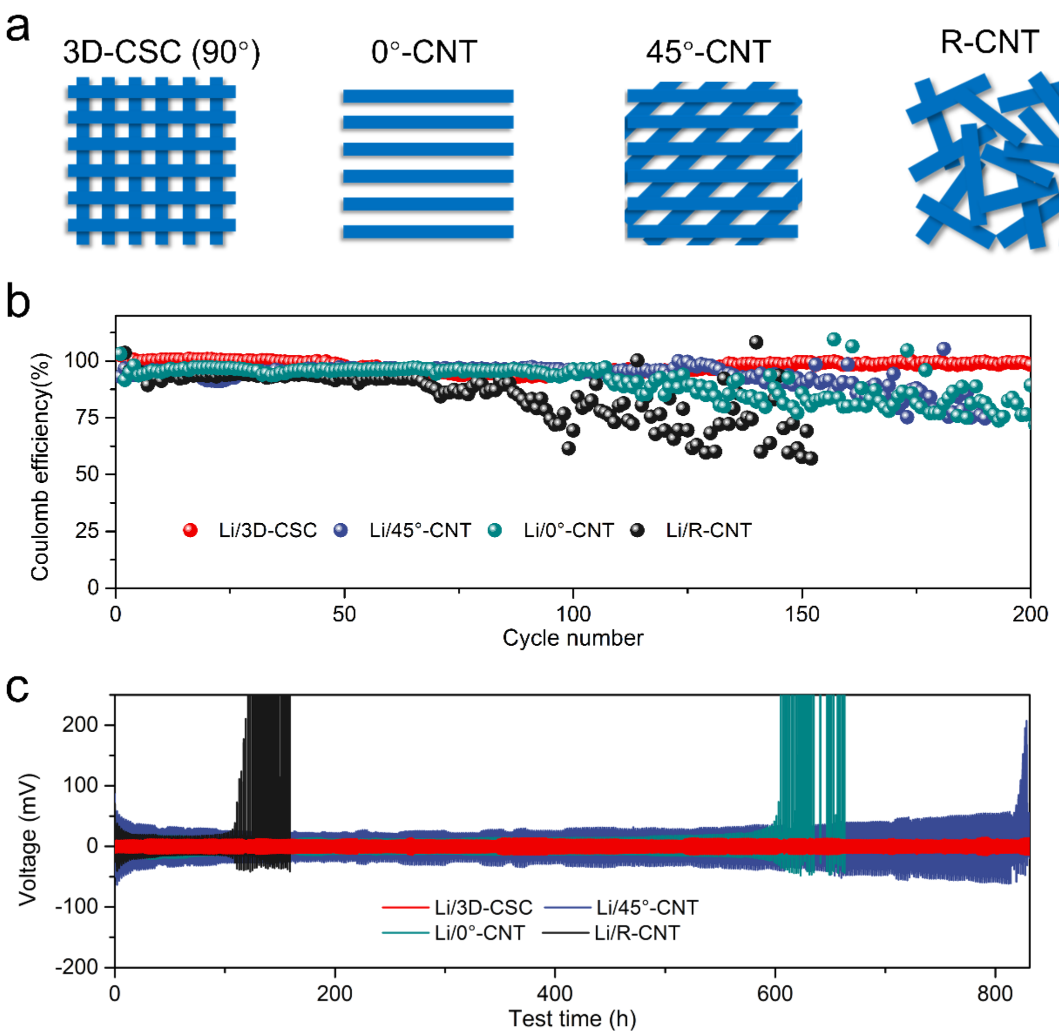

Figure S27. **a**, Schematics of different CNT scaffolds prepared for control experiments. **b**, CE evolution of four paradigms of CNT-based scaffolds. **c**, Overpotential evolution of four paradigms of CNT-based scaffolds.

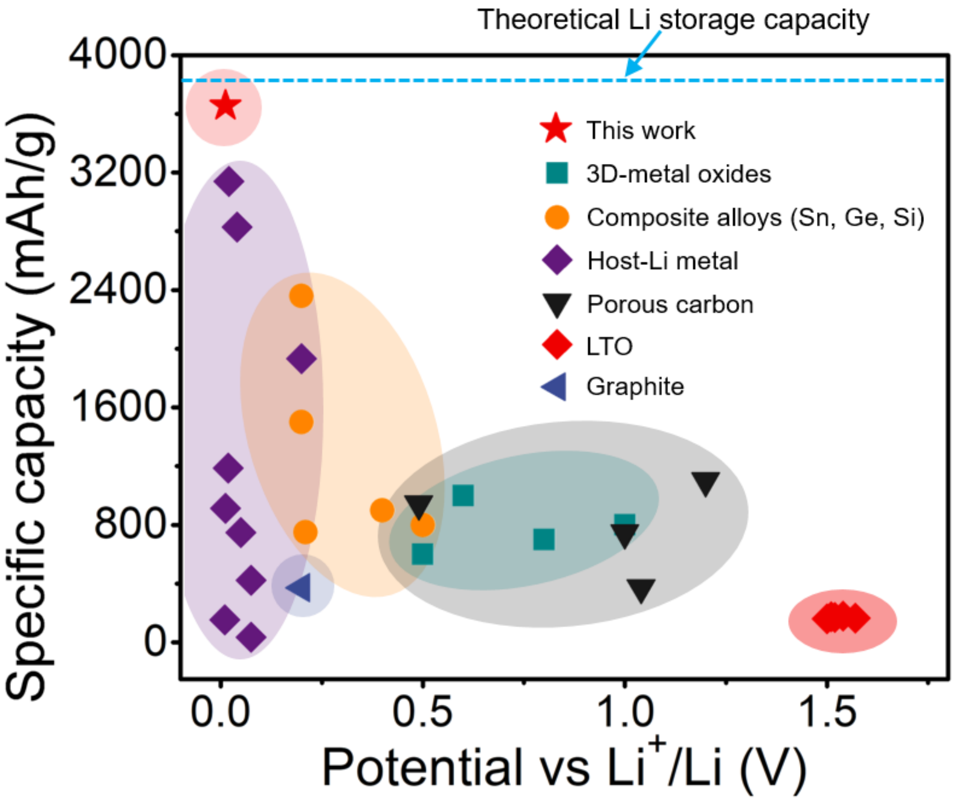

Figure S28. Comparison of the specific gravimetric capacity of the Li/3D-CSC with the other anodes for lithium batteries including 3D-metal oxides,[S1] composite alloys,[S2-6] host-Li metal,[S7-15] porous carbon,[S16-19] LTO[S20-23] and graphite.[S24] The Li/3D-CSC anode presented the highest gravimetric capacity of 3656 mAh/g which was very close to the theoretical capacity of metal Li (3860 mAh/g).

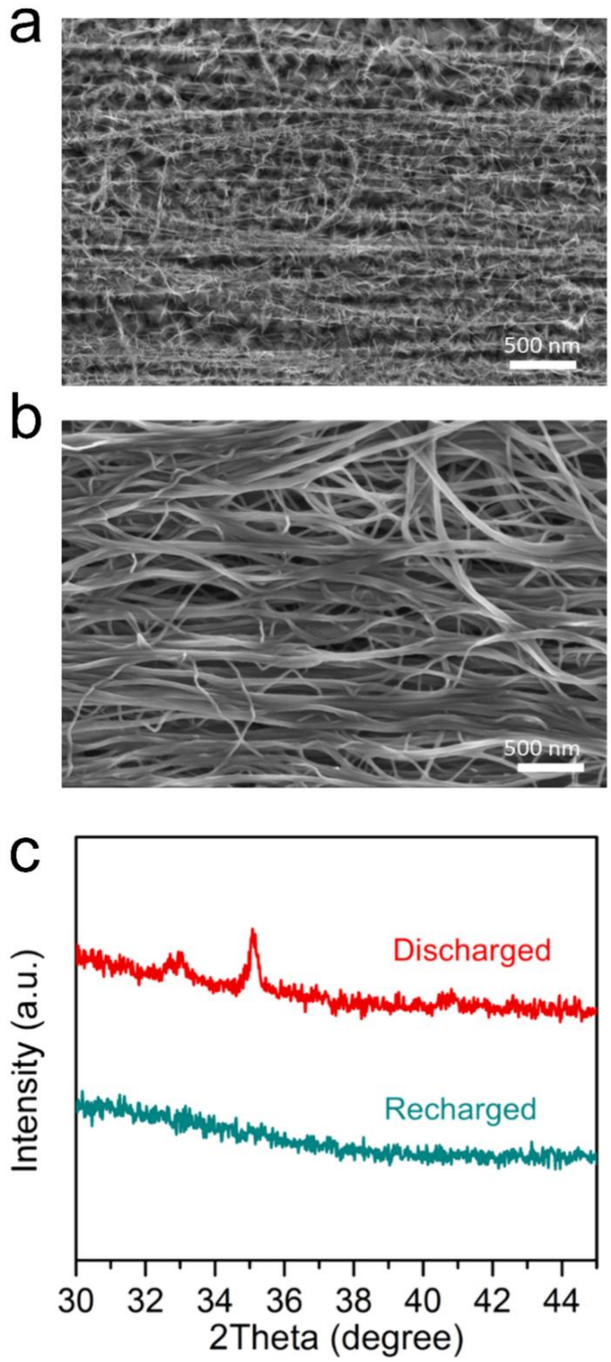

Figure S29. a and **b**, SEM images of the cathode after discharging and recharging, respectively. **c**, XRD patterns of the Li-O_2 battery cathodes at discharged and recharged states. The peak from discharged profile was assigned to Li_2O_2.

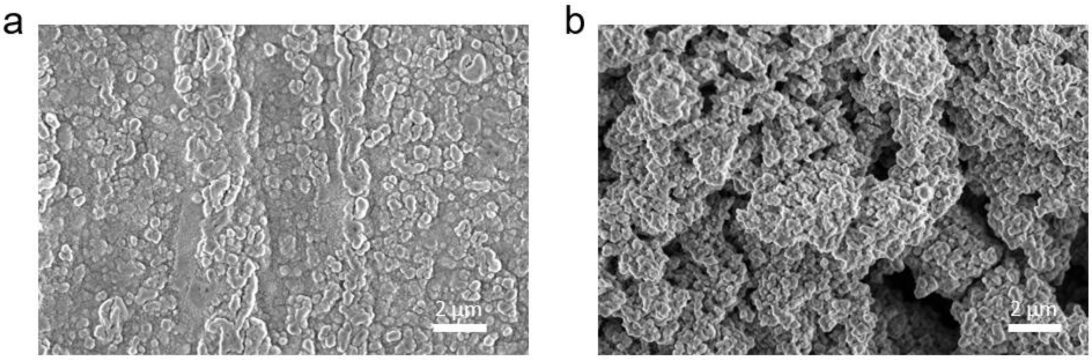

Figure S30. a and **b**, High-magnification SEM images showing the morphology of Li/3D-CSC and bare Li anodes after cycling, respectively.

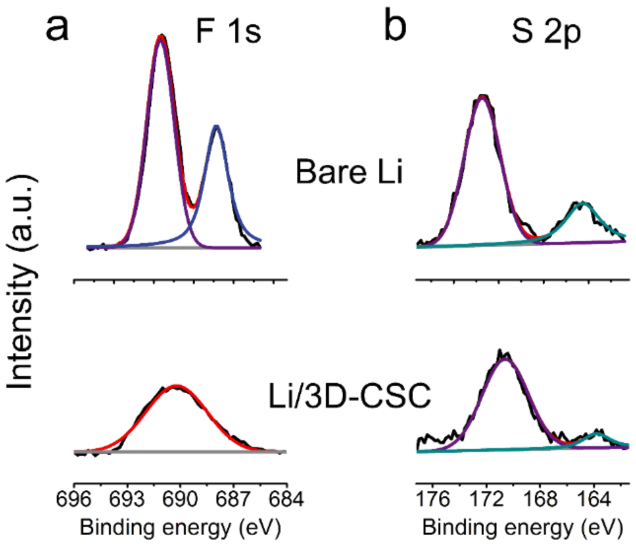

Figure S31. a and **b**, F 1s and S 2p XPS analysis of SEI films on routine Li and Li/3D-CSC anodes in Li-O_2 batteries after cycling, respectively.

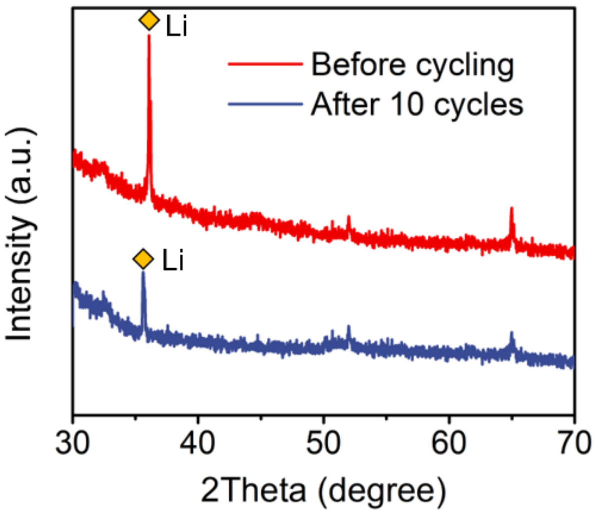

Figure S32. XRD patterns of the Li/3D-CSC in Li-O_2 batteries before and after cycling.

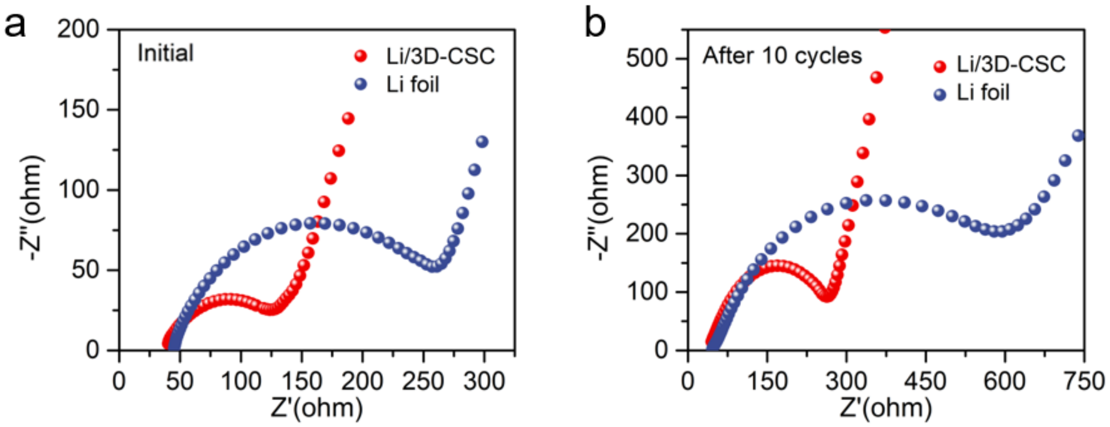

Figure S33. a and **b**, Electrochemical impedance spectra of Li-O_2 full batteries based on Li/3D-CSC and bare Li anodes before and after cycling, respectively.

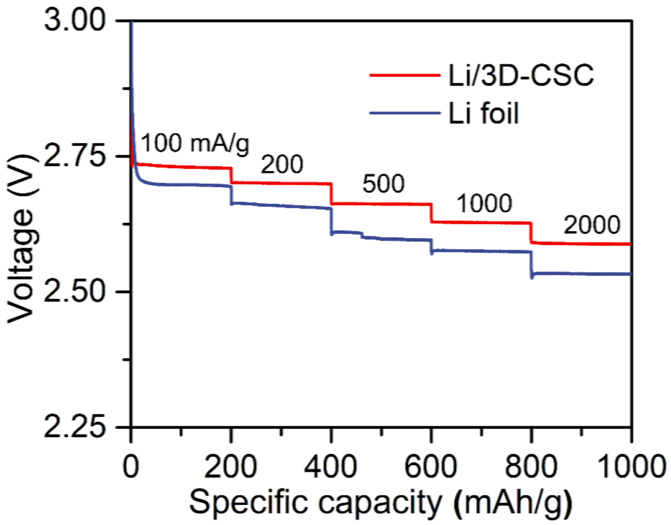

Figure S34. Rate performance of the Li-O_2 batteries with Li/3D-CSC and bare Li foil anodes.

Supplementary Tables

Table S1. The elemental composition variations extracted from X-ray photoelectron spectroscopy analysis characterizations of Li/3D-CSC and Li/Cu foil anodes during different stages (I, after activation process; II, after first cycle of Li deposition and III, after 50 cycles of Li plating/stripping).

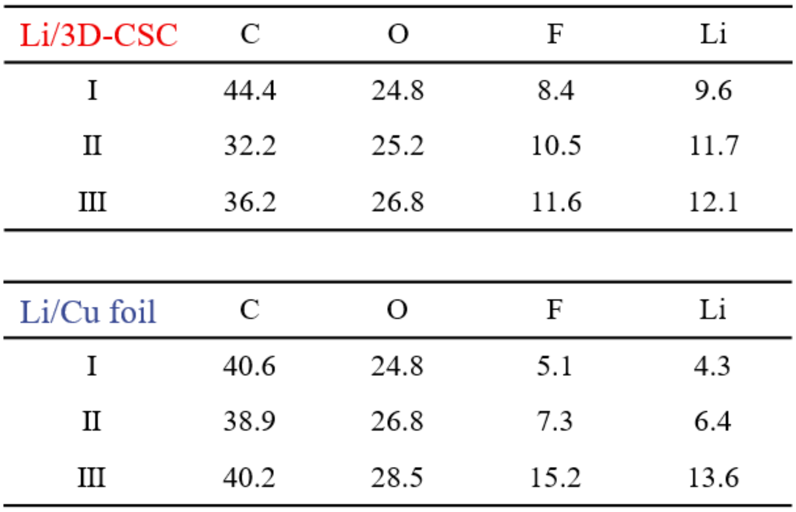

Li/3D-CSC	C	O	F	Li
I	44.4	24.8	8.4	9.6
II	32.2	25.2	10.5	11.7
III	36.2	26.8	11.6	12.1

Li/Cu foil	C	O	F	Li
I	40.6	24.8	5.1	4.3
II	38.9	26.8	7.3	6.4
III	40.2	28.5	15.2	13.6

Table S2. Comparison of typical parameters and specific capacities of representative carbon-based host for lithium anodes.

Ref	Initial thickness	Mass density	Gravimetric capacity	Areal capacity	Rate performance
S7	50 μm	0.05 mg/cm^3	748 mAh/g	4 mAh/cm^2	10 mA/cm^2
S8	108 μm	~108 mg/cm^3	913 mAh/g	10 mAh/cm^2	10 mA/cm^2
S9	200 μm	3-3.5 mg/cm^2	1187.9 mAh/g	6 mAh/cm^2	2 mA/cm^2
S10	150 μm	0.392 mg/cm^2	422.5 mAh/g	2 mAh/cm^2	-
S11	800 μm	26 mg/cm^2	1932 mAh/g	-	5 mA/cm^2
S12	43 μm	19.4 mg/cm^2	153.6 mAh/g	0.5 mAh/cm^2	-
S13	-	1.13 mg/cm^2	722 mAh/g	1 mAh/cm^2	1 mA/cm^2
S14	~100 μm	0.63 mg/cm^2	up to 3140 mAh/g	10 mAh/cm^2	10 mA/cm^2
S15	12 μm	0.68 mg/cm^2	2830 mAh/g	10 mAh/cm^2	10 mA/cm^2
This work	**1.1-3.3 μm**	**0.07-0.21 mg/cm^2**	**up to 3656 mAh/g**	**up to 12 mAh/cm^2**	**10 mA/cm^2**

Supplementary References:

S1. P. Poizot, S. Laruelle, S. Grugeon, L. Dupont, J-M. Tarascon, *Nature* **2000**, *407*, 496-499.

S2. T. Kennedy, E. Mullane, H. Geaney, M. Osiak, C. O' Dwyer, K. M. Ryan, *Nano Lett.* **2014**, *14*, 716-723.

S3. M. Halim, C. Hudaya, A. Y. Kim, J. K. Lee, *J. Mater. Chem. A* **2016**, *4*, 2651-2656.

S4. S. Choi, T. W. Kwon, A. Coskun, J. W. Choi, *Science* **2017**, *357*, 279-283.

S5. W. Zhang, *J. Power Sources* **2011**, *196*, 13-24.

S6. Z. Lu, N. Liu, H. Lee, J. Zhao, W. Li, Y. Li, C. Yi, *ACS Nano* **2015**, *9*, 2540-2547.

S7. A. O. Raji, S. R. Villegas, N. D. Kim, X. Fan, Y. Li, S. Gal, J. Sha, J. M. Tour, *ACS Nano* **2017**, *11*, 6362-6369.

S8. S. Jin, Z. Sun, Y. Guo, Z. Qi, C. Guo, X. Kong, Y. Zhu, H. Ji, *Adv. Mater.* **2017**, *29*, 1700783-1700789.

S9. L. Liu, Y. Yin, J. Li, N. Li, X. Zeng, H. Ye, Y. Guo, L. Wan, *Joule* **2017**, *1*, 563-575.

S10. R. Zhang, X. Chen, X. Chen, X. Cheng, X. Zhang, C. Yan, Q. Zhang, *Angew. Chem. Int. Ed.* **2017**, *129*, 7764-7768.

S11. S. Chi, Y. Liu, W. Song, L. Fan, Q. Zhang, *Adv. Funct. Mater.* **2017**, *27*, 1700348-1700357.

S12. C. Yang, Y. Yin, S. Zhang, N. Li, Y. Guo, *Nat. Commun.* **2015**, *6*, 8058-8066.

S13. K. Xie, W. Wei, K. Yuan, W. Lu, M. Guo, Z. Li, Q. Song, X. Liu, J. Wang, C. Shen, *ACS Appl. Mater. Interfaces* **2016**, *8*, 26091-26097.

S14. L. Liu, Y. I. Yin, J. I. Li, S. U. Wang, Y. U. Guo, L. U. Wan, *Adv. Mater.* **2018**, *30*, 1706216-1706223.

S15. Z. Sun, S. Jin, H. Jin, Z. Du, Y. Zhu, A. Cao, H. Ji, L. Wan, *Adv. Mater.* **2018**, 1800884-1800890.

S16. L. Qie, W. Chen, Z. Wang, Q. Shao, X. Li, L. Yuan, X. Hu, W. Zhang, Y. Huang, *Adv. Mater.* **2012**, *24*, 2047-2050.

S17. A. D. Roberts, X. Li, H. Zhang, *Chem. Soc. Rev.* **2014**, *45*, 4341-4356.

S18. A. D. Roberts, S. Wang, X. Li, H. Zhang, *J. Mater. Chem. A* **2014**, *2*, 17787-17796.

S19. H. Zhou, S. Zhu, M. Hibino, I. Honma, M. Ichihara, *Adv. Mater.* **2010**, *15*, 2107-2111.

S20. Y. Tang, L. Yang, Z. Qiu, J. Huang, *J. Mater. Chem.* **2009**, *19*, 5980-5984.

S21. Y. Wang, L. Gu, Y. Guo, H. Li, X. He, S. Tsukimoto, Y. Ikuhara, L. Wan, *J. Am. Chem. Soc.* **2012**, *134*, 7874-7879.

S22. L. Shen, E. Uchaker, X. Zhang, G. Cao, *Adv. Mater.* **2012**, *24*, 6502-6506.

S23. S. Chen, Y. Xin, Y. Zhou, Y. Ma, H. Zhou, L. Qi, *Energy Environ. Sci.* **2014**, *7*, 1924-1930.

S24. N. Nitta, F. Wu, J. Lee, G. Yushin, *Mater. Today* **2015**, *18*, 252-264.

S25. Z. Zhao, J. Huang, Z. Peng, *Angew. Chem. Int. Ed.* **2018**, *57*, 3874-3886.